Earthquakes and Structures, Vol. 2, No. 3 (2011) 233-256
DOI: http://dx.doi.org/10.12989/eas.2011.2.3.233

Applicability of Cu-Al-Mn shape memory alloy bars to retrofitting of historical masonry constructions

Kshitij C. Shrestha[1], Yoshikazu Araki*[1], Takuya Nagae[2], Toshihiro Omori[3],
Yuji Sutou[3], Ryosuke Kainuma[3] and Kiyohito Ishida[3]

[1]*Department of Architecture and Architectural Engineering, Graduate School of Engineering,*
Kyoto University, Katsura, Nishikyo, Kyoto 615-8540, Japan
[2]*E-Defense, National Research Institute for Earth Science and Disaster Prevention,*
Shinjimicho, Miki, Hyogo 673-0515, Japan
[3]*Department of Materials Science, Graduate School of Engineering, Tohoku University,*
Aoba-yama 6-6-02, Sendai 980-8579, Japan

(Received December 6, 2010, Accepted February 11, 2011)

Abstract. This paper investigates the applicability of newly developed Cu-Al-Mn shape memory alloy (SMA) bars to retrofitting of historical masonry constructions by performing quasi-static tests of half-scale brick walls subjected to cyclic out-of-plane flexure. Problems associated with conventional steel reinforcing bars lie in pinching, or degradation of stiffness and strength under cyclic loading, and in their inability to restrain residual deformations in structures during and after intense earthquakes. This paper attempts to resolve the problems by applying newly developed Cu-Al-Mn SMA bars, characterized by large recovery strain, low material cost, and high machinability, as partial replacements for steel bars. Three types of brick wall specimens, unreinforced, steel reinforced, and SMA reinforced specimens are prepared. The specimens are subjected to quasi-static cyclic loading up to rotation angle enough to cause yielding of reinforcing bars. Corresponding nonlinear finite element models are developed to simulate the experimental observations. It was found from the experimental and numerical results that both the steel reinforced and SMA reinforced specimens showed substantial increment in strength and ductility as compared to the unreinforced specimen. The steel reinforced specimen showed pinching and significant residual elongation in reinforcing bars while the SMA reinforced specimen did not. Both the experimental and numerical observations demonstrate the superiority of Cu-Al-Mn SMA bars to conventional steel reinforcing bars in retrofitting historical masonry constructions.

Keywords: unreinforced masonry; superelasticity; Cu-Al-Mn shape memory alloy; steel reinforcement; out-of-plane flexure; finite element modeling.

1. Introduction

Unreinforced masonry (URM) walls in historical masonry constructions are prone to failure during high or even moderate intensity earthquakes. Recognizing the shortcomings of URM walls, there has been a surge in interest in developing techniques for improving their seismic behavior (Karantoni and Fardis 1992, Ehsani *et al.* 1999, ElGawady *et al.* 2004, Abrams *et al.* 2007, Willis *et*

---

* Corresponding author, Associate Professor, E-mail: araki@archi.kyoto-u.ac.jp

al. 2010). Main techniques devised in the studies can be classified in the following types: (1) attachment of reinforcing members, (2) surface treatment, (3) grout injection, (4) post-tensioning, and (5) reinforced core technique.

Attachment of steel or reinforced concrete members to URM walls and partial replacement of URM walls by steel or reinforced concrete members, shown in Fig. 1(a), are one of the most common retrofitting techniques. Adhesion of fiber reinforced plastic overlays shown in Fig. 1(b) or spraying concrete layers over a mesh of steel reinforcing bars shown in Fig. 1(c) are representative examples of surface treatment. Although these techniques give higher seismic resistance to URM walls, they may change the appearance of URM constructions significantly and may cease their aesthetic value. This is problematic especially when retrofitting historical masonry constructions.

On the other hand, grout injection, post-tensioning, and reinforced core techniques do not change the outlook of URM walls. Nevertheless, the increase of strength obtained by injecting grout into voids of URM walls is uncertain, and no increase can be obtained in ductility. Post-tensioning is effective when masonry material is strong and stiff enough. Otherwise, stress relaxation and anchorage may become problematic, which is often the case in retrofitting historical masonry constructions. Reinforced core technique, wherein reinforcing steel bars are inserted vertically into holes drilled at the center of URM walls as shown in Fig. 1(d), is often suitable for retrofitting historical masonry constructions because the technique does not change the appearance of URM walls and enhances both strength and ductility (Plecnik *et al.* 1986, Abrams *et al.* 2007). In reinforced core technique, however, the use of steel bars as reinforcing elements may lead to pinching, or degradation of stiffness and strength under cyclic loading. Pinching is caused by inelastic elongation of reinforcing steel bars and may lead to zero stiffness in a wide deformation range around the initial configuration (Button and Mayes 1992) or to large residual deformation during and after intense earthquakes. These unstable states increase collapse potential of masonry walls. Moreover, it becomes difficult to repair with minor interventions like inserting grouts into mortar joints.

To overcome the difficulties mentioned above, there is an increasing interest in application of shape memory alloys (SMAs) to retrofitting of historical masonry constructions (Mazzolani and Mandara 2002, Desroches and Smith 2004, Song *et al.* 2006). The first known example of SMAs applied in a retrofit project of a historical masonry construction is done by Indirli *et al.* (2001) on S. Giorgio Church Bell Tower. The rehabilitation process involved post tensioning using devices with SMA wires of 1 mm diameter. After this project, SMA wires were applied to several retrofitting projects of existing historical masonry constructions (Paret *et al.* 2008, Christis *et al.* 2008, Martelli 2008).

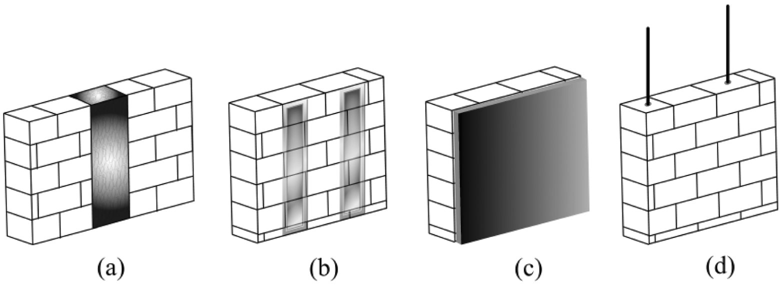

Fig. 1 Masonry wall retrofitting techniques: (a) attachment of reinforcing members, (b) FRP surface overlays, (c) shotcrete and (d) reinforced core technique

SMAs with superelasticity, or shape recovery property on unloading, are attractive in retrofitting of historical masonry constructions because they dissipate energy, limit force transmissions, and reduce or eliminate residual deformations. These characteristics stabilize retrofitted historical masonry constructions during and after intense earthquakes. The first and second characteristics are suitable for enhancing the problems associated with post-tensioning using high-strength steel rods. The third characteristic can be applied to resolve pinching problems associated with reinforced core technique. In most studies and projects conducted so far, Ni-Ti SMAs were applied to retrofitting of historical masonry constructions because of their superior mechanical properties to other SMAs. Nevertheless, high material cost and machining difficulty of Ni-Ti SMAs hinder their wide-spread use in retrofitting of historical URM constructions.

As an alternative class of SMAs, application of Cu-Al-Be SMAs to retrofitting of historical masonry constructions was studied because of their lower cost and higher machinability (El-Borgi *et al*. 2008). To the authors' knowledge, however, superelasticity of Cu-Al-Be SMAs is significantly inferior to, about half of, that of Ni-Ti SMAs. Moreover, beryllium and beryllium compounds have potential risks to human health unless properly handled. As another class of SMAs, development of Cu-Al-Mn SMAs is underway (Sutou *et al*. 2003, Sutou *et al*. 2005). The superelasticity of Cu-Al-Mn SMAs is comparable to Ni-Ti SMAs, and Cu-Al-Mn SMAs have essentially no risks to human health. Nevertheless, the diameter of the Cu-Al-Mn SMA wires produced were limited to be less than or equal to 1.5 mm due to the dependence of superelasticity on grain size. Recently, Araki *et al*. (2010) have succeeded to obtain Cu-Al-Mn SMA bars with diameters of 4 mm and 8 mm whose superelasticity is comparable to Ni-Ti SMA bars by making grain sizes large enough.

In this paper, applicability of newly developed Cu-Al-Mn SMA bar is examined to retrofitting of historical URM constructions. Although superelasticity of Cu-Al-Mn SMA is not superior to that of Ni-Ti SMAs, Cu-Al-Mn SMA is superior from the viewpoints of machinability, cold workability, and material cost. These characteristics make Cu-Al-Mn SMA a strong candidate for practical seismic applications. In this paper, a series of quasi-static cyclic out-of-plane tests are conducted to accumulate test data of SMA reinforced masonry (SMA-RM) as well as URM and steel reinforced masonry (ST-RM) constructions. FEM models are developed in reference to the mechanism obtained from the test results. The developed FEM models form a basis for identifying the performance of real SMA-RM constructions.

2. Experiments

2.1 Specimens and materials

Fig. 2 shows the geometry of a brick wall specimen. A single-wythe brick wall specimen was constructed respectively for the URM, ST-RM and SMA-RM wall. The wall specimen represents a top storey gable wall with low level of anchorage system between the wall and the top support making the wall fail in cantilever action. Half-scaled bricks of 95 mm × 53 mm × 31 mm were used to construct the wall specimens. The bricks have holes for inserting bars in case of the reinforced specimens. For the reinforced masonry specimens, 2 reinforcing bars with 4 mm diameter were inserted at the spacing of 150 mm. The reinforcement design satisfies the minimum requirement of reinforcement in European Standard (Eurocode 8 2004). Fig. 3 shows the procedures involved in the reinforced specimen preparation. Fig. 3(a) shows a SMA bar after threading. Threading of SMA

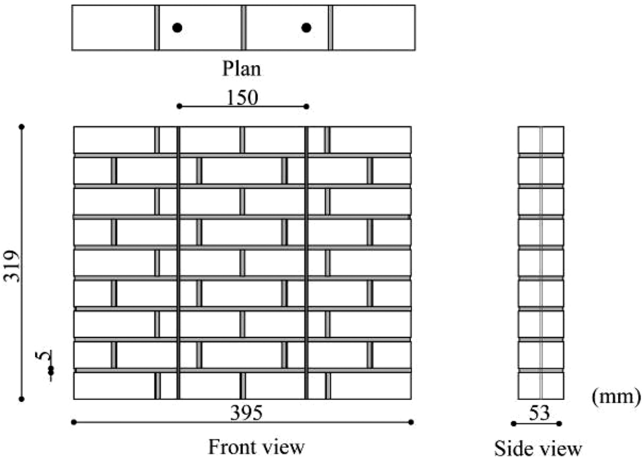

Fig. 2 Geometry of a brick wall specimen

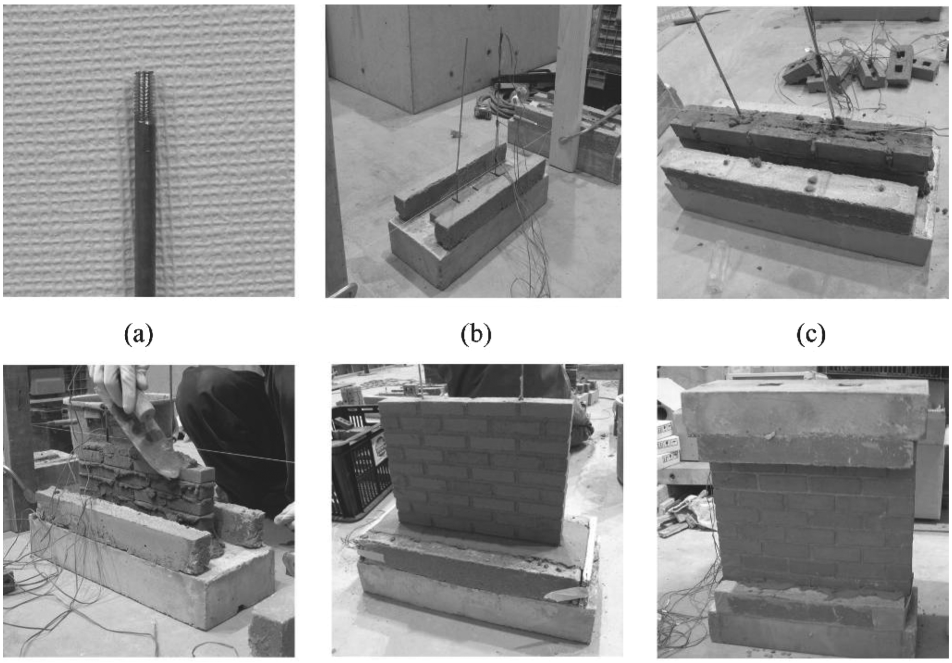
(a) (b) (c)
(d) (e) (f)

Fig. 3 Processes involved during specimen preparation: (a) threaded SMA bar, (b) concrete block with SMA bar inserted, (c) position of coupler connecting SMA bar and stainless steel bar, (d) brick laying, (e) completion of brick laying and (f) placement of concrete block support on the top of specimen

bars was as easy as normal steel, which is a distinct characteristic of Cu-Al-Mn SMAs compared to Ni-Ti SMAs. As shown in Figs. 3(b) to 3(e), the specimen was constructed on a concrete block by professional masons. After placing another concrete block on the specimen as shown in Fig. 3(f), bolts were tightened lightly at the both ends of reinforcing bars to fix the brick wall specimen to the concrete blocks.

Table 1 Material properties of brick and mortar

	Masonry prism f_c (MPa)	Brick unit f_c (MPa)	Mortar cube f_c (MPa)	Masonry prism f_t (MPa)	Mortar bar f_t (MPa)
Method	LUMB 1 (RILEM 1994)	ASTM C 67-07 (ASTM 2007)	ASTM C 1019-05 (ASTM 2007)	ASTM E 518-03 (ASTM 2007)	ASTM C 580-02 (ASTM 2007)
Mean	13.52	35.79	18.40	0.47	4.50
Deviation	3.13	6.57	0.17	0.22	0.15

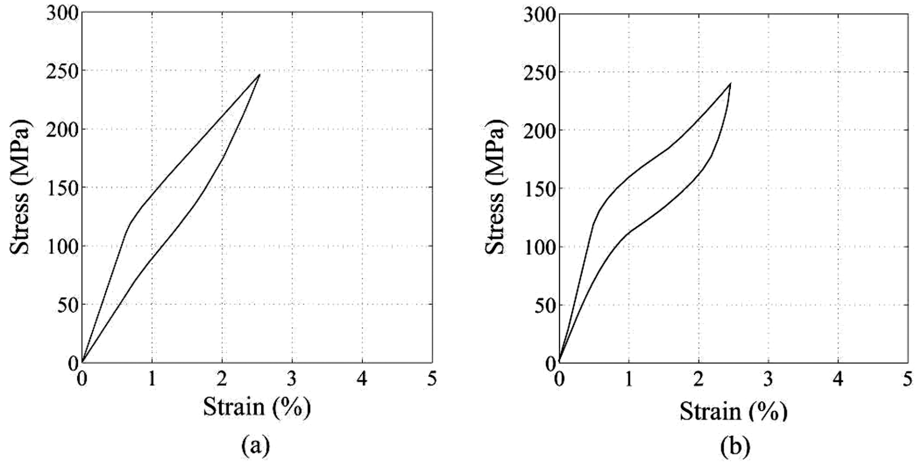

Fig. 4 Stress-strain relations after training for (a) SMA bar 1 and (b) SMA bar 2

Table 1 shows the mean and standard deviation values obtained from the material tests of bricks, mortars, and masonry prisms for compressive strength f_c and tensile strength f_t (RILEM 1994, ASTM 2007). The composition of water, cement, and sand for the mortar was 1:1:4.5. JIS SS400 steel bars of 4 mm diameter were used in the ST-RM specimens. Tensile tests done on SS400 steel bars gave yield stress and strength of about 200 MPa and 400 MPa respectively. For the SMA-RM specimens, Cu-Al-Mn SMA bars with 160 mm length were used only at the lower portion of the SMA-RM wall specimen. The upper portion of the reinforcing bar was SUS304 stainless steel, whose nominal strength is 520 MPa.

Cu-16.7 at.%Al-11.6 at.%Mn alloy was prepared by Furukawa Techno Material Co., Ltd, where SMA bars with diameters of 4 mm were obtained by hot forging and cold drawing. The solution treatment was conducted at 900°C, followed by quenching in water, and they were subsequently aged at 200°C to stabilize superelastic property. The SMA bars were trained beforehand up to strain of 3% by applying quasi-static cyclic loading before inserting them into brick wall specimens. Stress-strain histories for the two SMA bars after training are shown in Fig. 4. From the figure, it can be seen that the yield, or forward transformation, stresses of the SMA bar are in the range between 120 MPa to 140 MPa. And the maximum stress experienced ranges from 240 MPa to 250 MPa. Both the SMA bars have the recovery strain of more than 2% after the training. It should be noted that strain observations made in Fig. 4 could possibly be overestimated due to cross-head measurements of strain. As a result, the initial modulus observed in Fig. 4 may be significantly less than the nominal value of SMAs.

2.2 Test setup and loading program

Fig. 5 shows the test arrangement. All the specimens were subjected to quasi-static cyclic loading using a hydraulic shaking table. As shown in Fig. 5(a), the lower concrete support was fixed to the shaking table using angle steel members, and a steel plate was fixed to the upper concrete block support to apply a constant vertical load. The mass of the steel plate was 145 kg. The average compressive stress at the base of the brick wall specimen was 0.08 MPa. Two roller supports were provided at the both sides of the steel plate as shown in Fig. 5(b). The support allowed vertical translation and rotation of the steel plate but did not allow horizontal translation. Displacement controlled cyclic ramp load was given by the shaking table so that the amplitude θ_a of the rotation angle of the wall specimen as shown in Fig. 5(a) was equal to 1/700, 1/350, 1/175, 1/116, 1/87, 1/70, 1/58, 1/44, 1/35 and 1/18 radian. The base displacement was applied at an average rate of 0.2 mm/sec to realize quasi-static loading. Laser displacement transducers were used to acquire displacement records during the experiment. Cross marks in Fig. 5(c) show the locations where displacements were measured. Strain data of reinforcing bars were measured using strain gages at the locations shown in Fig. 5(c).

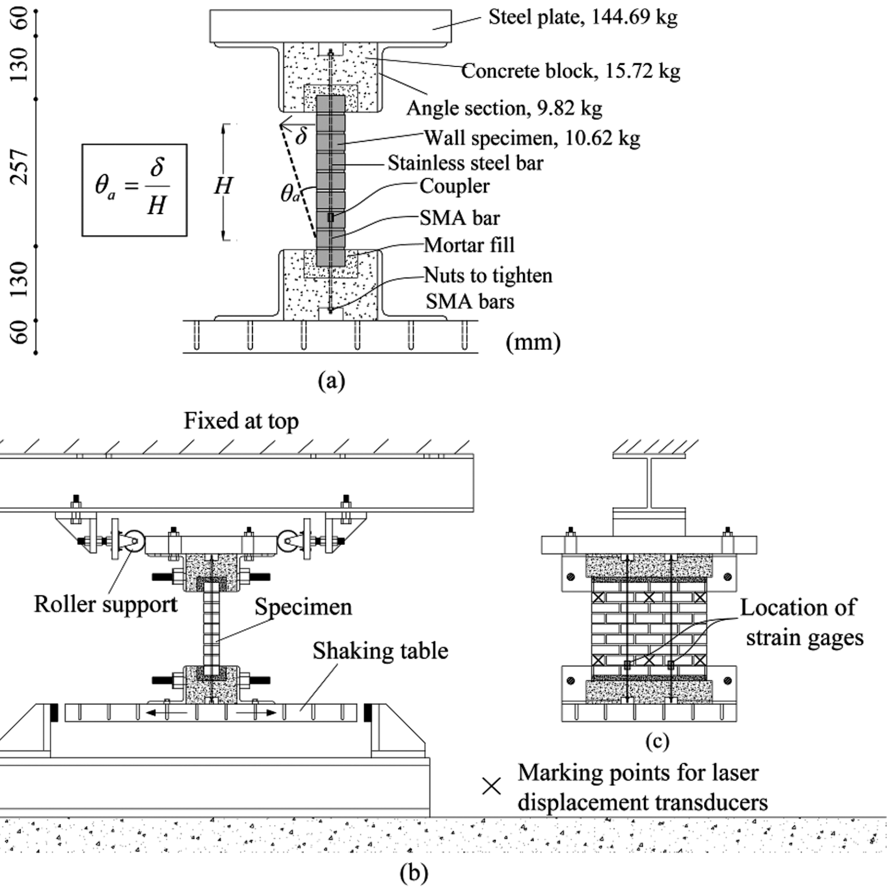

Fig. 5 Out-of-plane test set-up on shaking table: (a) specimen with its major components, (b) test set-up and (c) front view showing laser displacement cross-marks

2.3 Results and discussions

2.3.1 URM specimen

The relationship between the horizontal resisting force and the rotation angle for the URM specimen is shown in Fig. 6. Fig. 7 shows the deformed shape and the bed joint cracking for the URM specimen. As seen from Fig. 6, the load-deformation response showed two distinct stages; the first was linear pre-cracking stage, and this was followed by the second stage with a descending curve. Fig. 6(a) shows the response when $\theta_a < 1/70$ radian. The pre-cracking response was almost linear until the peak force was observed. After the peak, the formation of the first crack was observed at the 1st mortar joint level from the bottom. The peak force represents the strength associated with the tensile cracking of the bed mortar joint. Fig. 6(b) shows the response including the range $\theta_a > 1/70$ radian. The post-cracking descending curve was nearly linear, where the

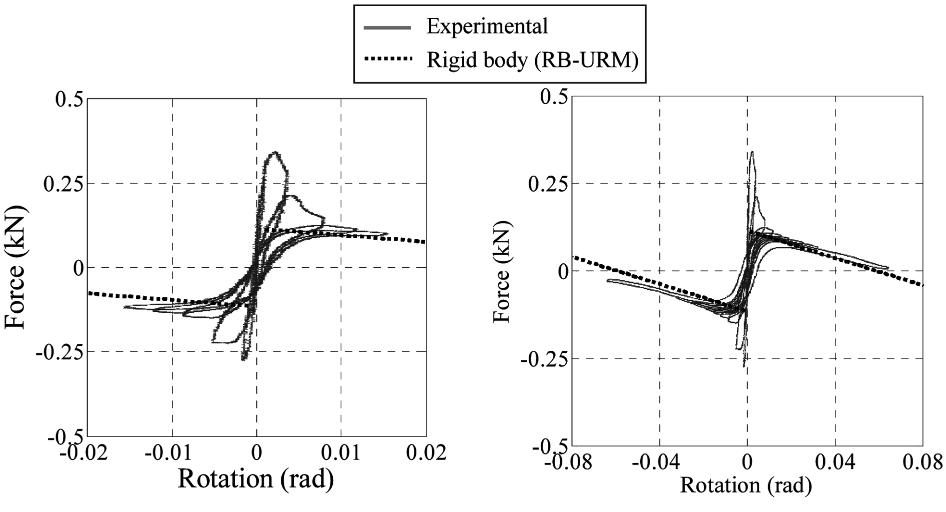

(a) (b)

Fig. 6 Force-rotation relation for the URM specimen: (a) $\theta_a < 1/70$ radian and (b) $\theta_a > 1/70$ radian

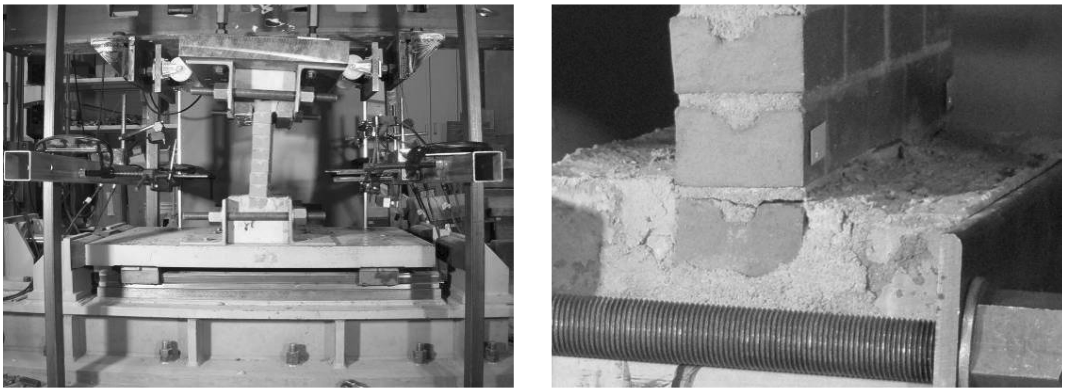

(a) (b)

Fig. 7 Deformed shapes for the URM specimen: (a) deformed shape and (b) bed joint cracking deformation continued to increase while the resisting force decreased up to the loss of horizontal resisting force.

The post-cracking response of the URM specimen can be reasonably predicted by a rigid body assumption (Griffith *et al*. 2004). The horizontal resistance F_C^U, assuming that the wall was cracked at the bed joint at the 1st mortar level from the bottom, is given by,

$$F_C^U = \frac{\left(\frac{t}{2} - h\theta\right)mg}{(h + t\theta)} \tag{1}$$

where t is the wall thickness, h is the height of the position of action of horizontal force measured from the 1st mortar joint level, θ is the rotation angle of the wall, m is the total mass of the steel plate, the upper concrete block, and the steel angle member, and g is the gravity acceleration. From Eq. (1), it is clear that the critical rotation angle θ_s for the loss of horizontal resistance is expressed as $\theta_s = t/(2h)$, which is around 0.06 radian. The dotted line in Fig. 6 shows that Eq. (1) predicts the post-cracking behavior reasonably well. As seen from the figure, after the first cracking of the wall, the force quickly dropped off and approached the prediction by the rigid body assumption.

2.3.2 ST-RM specimen

Fig. 8 illustrates the resisting force-rotation angle relationship. As shown in Fig. 8, the horizontal resisting force-rotation angle relationship of the ST-RM specimen was characterized by three distinct stages: (1) the pre-cracking stage, for $\theta_a < 1/175$ radian, (2) the post-cracking stage, for $1/175 < \theta_a < 1/58$ radian, and (3) the large deformation stage, for $\theta_a > 1/58$ radian. First, for $\theta_a < 1/175$ radian, similar to the URM specimen, almost linear pre-cracking stage was seen with the peak horizontal resisting force corresponding to the bed joint tensile strength as shown in Fig. 8(a). With the completion of the pre-cracking stage, the ST-RM specimen showed significant deformation with no real increase in the resisting force as seen in Fig. 8(b). Large difference between the un-cracked

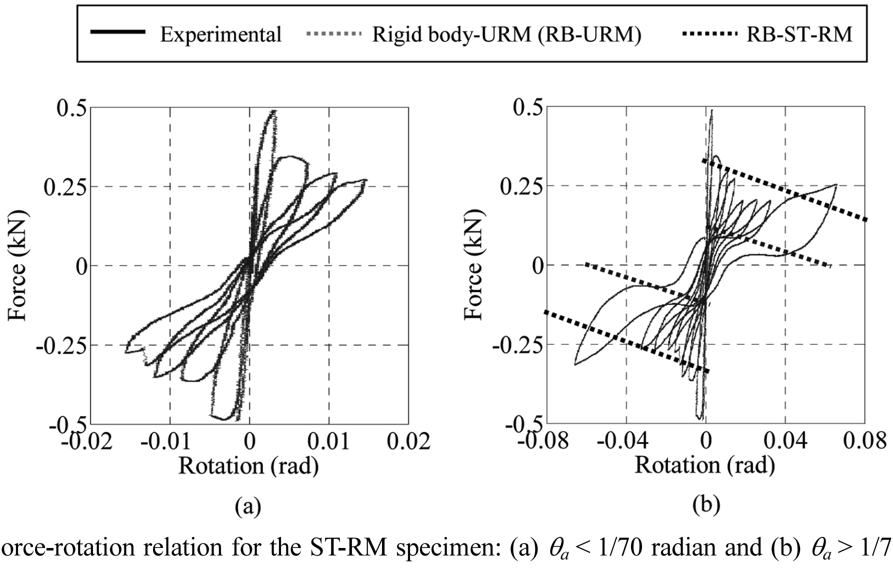

(a) (b)

Fig. 8 Force-rotation relation for the ST-RM specimen: (a) $\theta_a < 1/70$ radian and (b) $\theta_a > 1/70$ radian and cracked wall stiffness resulted in a continuous decrease in the resisting force measured. Fig. 8(b) also shows typical pinching phenomenon for the ST-RM specimen in the large deformation range. Detailed discussion on this issue is given later in Section 3.2.2.

The post-cracking response of ST-RM specimen is compared with a rigid body assumption as shown in Fig. 8(b). The horizontal resistance F_C^{ST} obtained from the rigid body model, assuming that the wall was cracked at the bed joint at the 1st mortar level from the bottom, is given by

$$F_C^{ST} = \frac{\left(\frac{t}{2} - h\theta\right)mg + F_p^{ST} \times \frac{t}{2}}{(h + t\theta)} \tag{2}$$

where F_p^{ST} is the strength of the reinforcing steel bar. The bar strength F_p^{ST} was computed using the yield stress of 210 MPa and the effective sectional area of the threaded portion of the steel bar, where the diameter was assumed to be 3 mm. The experimental response and the prediction by the rigid body assumption agree reasonably well as shown in Fig. 8(b).

2.3.3 SMA-RM specimen

As shown in Fig. 9, the horizontal resisting force-rotation angle response of the SMA-RM wall specimen showed behavior with three different stages. The pre- and post-cracking stages were similar to those of the ST-RM specimen. On the other hand, the large deformation stage showed major distinct features as compared to that of the ST-RM specimen. During the unloading phase, the behavior was particularly different with no pinching phenomenon. Also during the loading phase, constant restoring force was observed beyond the rotation angle of 0.04 radian. More details on these features are discussed later in Section 3.2.3.

The post-cracking response of SMA-RM specimen is also compared with the prediction by the rigid body assumption as shown in Fig. 9(b). Similar to the ST-RM specimen, the horizontal resistance obtained from the rigid body assumption is given by,

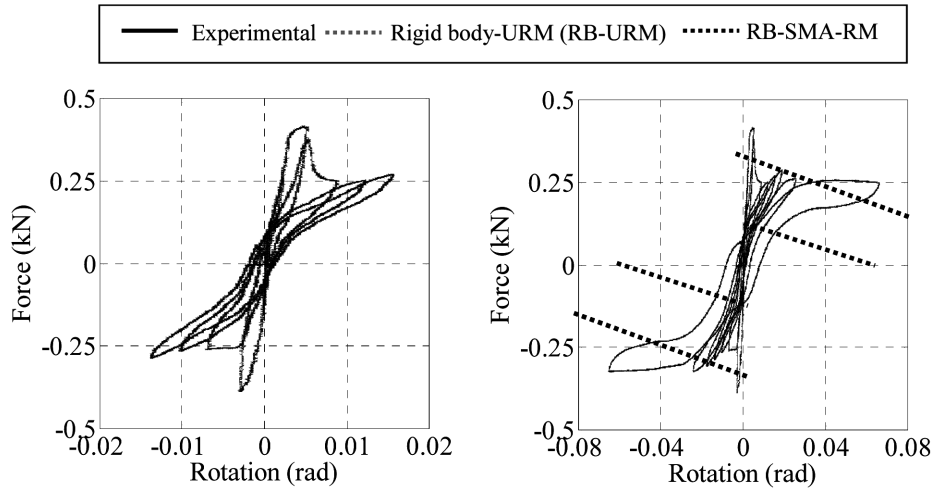

(a) (b)

Fig. 9 Force-rotation relation for the SMA-RM specimen: (a) $\theta_a < 1/70$ radian and (b) $\theta_a > 1/70$ radian

$$F_C^{SMA} = \frac{\left(\frac{t}{2} - h\theta\right) mg + F_p^{SMA} \times \frac{t}{2}}{(h + t\theta)} \tag{3}$$

where F_p^{SMA} is the strength of the reinforcing SMA bar assuming the maximum stress of 210 MPa. Here, 3 mm diameter of effective cross sectional area of the SMA bar is taken for representing the threaded portions. The results obtained from the experimental observation agree reasonably well with the rigid body assumption as shown in Fig. 9(b).

3. FE Modeling

3.1 Model generation

Masonry walls subjected to out-of-plane loading experience predominantly tensile failure in mortar joints. The out-of-plane response of URM walls is highly nonlinear and is often governed primarily by cracking at mortar joints and rocking resistance due to gravity rather than compressive failure of masonry and mortar materials. Masonry walls can be represented with significant simplification with entire mortar joint by interface element (Lourenco and Rots 1997). With this approach, the failure of brick-mortar interface is not distinguished from that of mortar layer itself. In this paper, complete FE models were generated and analyzed using the general purpose FE program DIANA9.3 (DIANA 2008). Masonry walls were modeled by assuming that brick units are fully elastic and material nonlinearity was concentrated on truss elements and interface elements. Rocking resistance due to gravity is incorporated by considering geometrical nonlinearity.

The FE model with the meshing adopted for the brick continuum elements and the interface

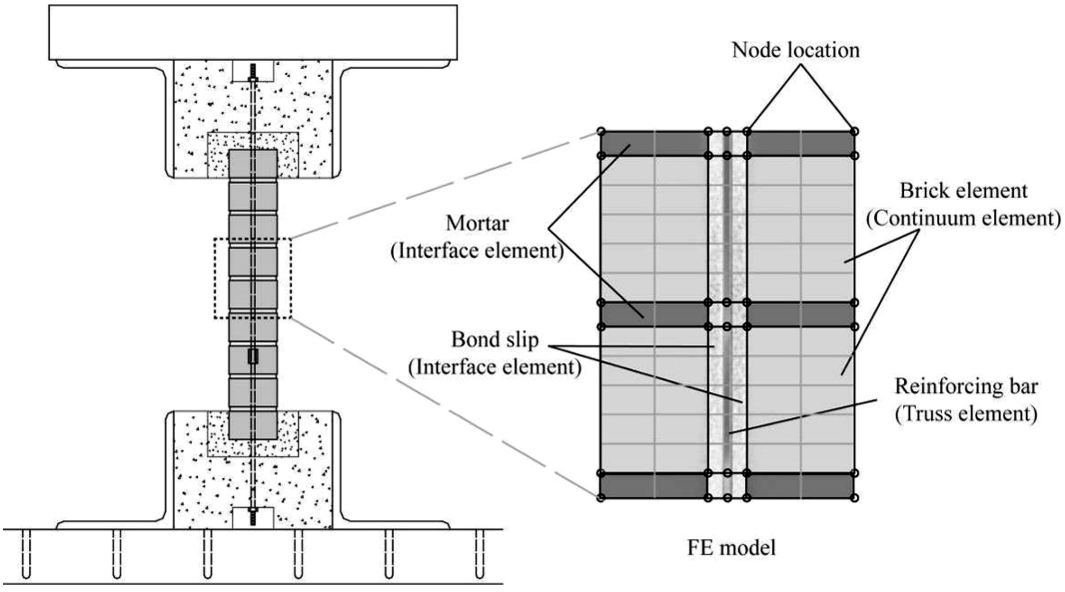

Fig. 10 FE mesh showing the brick unit, mortar interface, bond slip interface and reinforcing truss element bar

elements are shown in Fig. 10. A masonry brick unit was modeled using rectangular continuum elements that were connected with vertical and horizontal interface elements representing mortar and bond slip interface. For the reinforced masonry wall specimens, truss elements with proper constitutive relations and interface elements representing the bond slip interface between reinforcement elements and masonry elements were used. The details of the elements used are described below.

3.1.1 Brick

As mentioned above, bricks were modeled to work perfectly elastic during the whole loading history and modeled with four-node quadrilateral continuum elements. Material properties used included Young's modulus $E_b = 12$ GPa, Poisson's ratio $\upsilon_b = 0.15$, and density, $\rho_b = 2000$ kg/m^3 taken for typical masonry bricks (Oliveira *et al.* 2006).

3.1.2 Interface

Entire mortar joint was represented by brick unit/mortar interface. The interface model used in this study is implemented in DIANA9.3 (DIANA 2008) as linear interface elements between two lines (2+2 nodes). The constitutive model adopts a discrete crack initiation criterion of normal traction characterized by full reduction of strength after the strength criterion has been violated. A discrete crack arises if the normal traction f_n exceeds the tensile strength of mortar, $f_t = 0.47$ MPa. The behavior can be written as

$$\frac{f_n(\Delta u_n)}{f_t} = \begin{cases} 1 & \text{if } \Delta u_n \leq 0 \\ 0 & \text{if } 0 < \Delta u_n < \infty \end{cases} \tag{4}$$

where Δu_n is the deformation in the direction of normal traction f_n. The normal stiffness of $D_{11} = 82$ N/mm^3 and the shear stiffness of $D_{22} = 36$ N/mm^3 were adopted for the brick/mortar interface (Lourenco and Rots 1997).

A special interface element, named as nut interface as shown in Fig. 11, was incorporated to simulate the contact between nuts and brick. This element was particularly important to represent the pinching mechanism of the ST-RM specimen. The nut interface element adopted a discrete crack initiation criterion of normal traction with brittle behavior similar to the one adopted for mortar as given in Eq. (4). Here, the material strength property with $f_t = 0.2$ MPa was used. The tensile strength of this interface element was kept low enough and calibrated suitably so as to result in the loss of contact, or crack initiation, during unloading.

The bond-slip interface between reinforcing elements and masonry elements were represented by two types of interface elements, named Bond 1 and Bond 2, as shown in Fig. 11. The bond slip model proposed by Dörr (DIANA 2008) was used. The model uses a polynomial relation between shear traction and slip which shows a limit if the slip is larger than a certain value dt^0. The formulation for shear traction t_t is given by a cubic function

$$t_t = \begin{cases} f_s\left(5\left(\frac{dt}{dt^0}\right) - 4.5\left(\frac{dt}{dt^0}\right)^2 + 1.4\left(\frac{dt}{dt^0}\right)^3\right) & \text{if } 0 \leq dt < dt^0 \\ 1.9 f_s & \text{if } dt \geq dt^0 \end{cases} \tag{5}$$

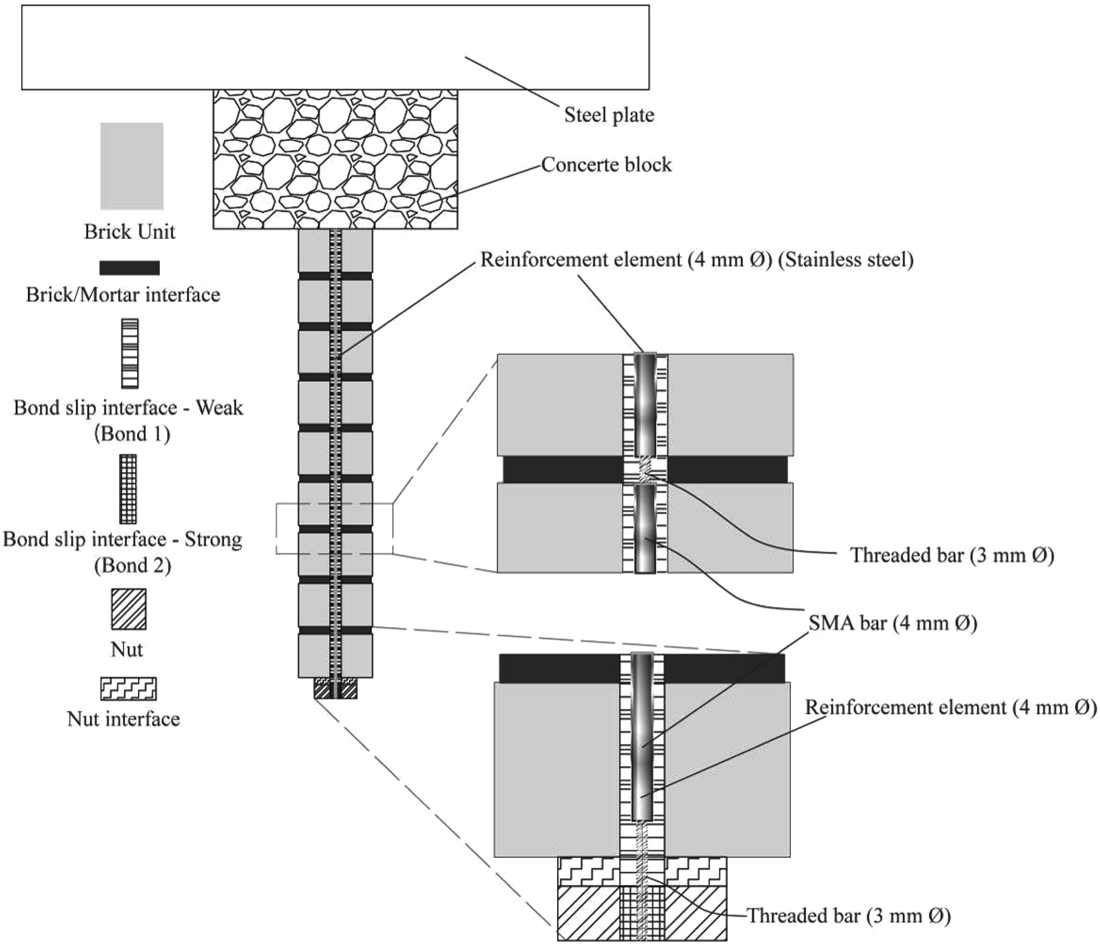

Fig. 11 FE model generation (SMA-RM model)

where f_s is the slip strength and dt^0 is the limiting slip distance. Unloading and reloading of the interface shear behavior is modeled using a secant approach as shown in Fig. 12.

FE model incorporates two bond-slip interfaces, one between the reinforcing elements and the masonry elements represented as Bond 1 and the other between reinforcing elements and nut represented by Bond 2 as shown in Fig. 11. The bond strength for Bond 1 interface was intentionally made very weak to allow slip of reinforcing elements with slip strength, $f_s = 0.1$MPa and limiting slip distance, $dt^0 = 0.06$ mm, where the slip strength parameter has been properly calibrated and kept sufficiently low so as to allow slip during unloading once the reinforcing bars get elongated. Additionally, a very strong bond slip interface was also included to resist the slip between the reinforcing bar and the nut at the bottom of the specimen in Bond 2. The slip strength property for this strong bond slip Bond 2 was taken to be 100 MPa which is strong enough to resist slip beyond the yield strength of the reinforcing bars used. The strength parameters for assigning bond-slip behavior have been calibrated appropriately so as to represent the experimental observations.

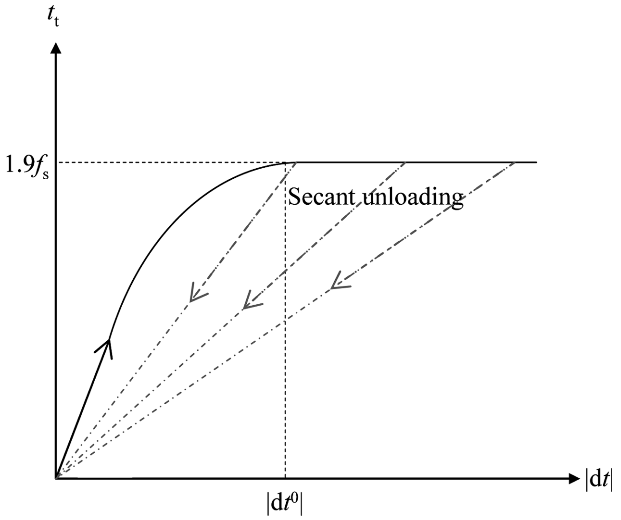

Fig. 12 Traction stress versus displacement plot with secant unloading for bond slip interface

3.1.3 Reinforcing bar

Steel reinforcements were represented by truss elements with material properties represented by suitable hardening parameters for JIS SS400 steel bars of diameter 3 mm representing the threaded portion of the bar. Isotropic hardening was assumed with hardening parameters as shown in Fig. 13(a) with yield stress of 180 MPa adopted with Young's modulus E_{st} = 200GPa. The tangent modulus of the second branch was taken to be 0.4% of the initial modulus up to maximum stress of 400 MPa and almost perfectly plastic beyond this stress level.

SMA bars were also represented by truss elements with its superelastic property incorporated by assuming tri-linear elastic constitutive model shown in Fig. 13(b). The initial modulus for SMA was E_{SMA} = 60 GPa up to yield stress of 120 MPa. The tangent modulus of the 2nd branch was taken to be 3% of initial tangent modulus up to stress of 230 MPa. And beyond this stress level, very low tangent modulus of 310 MPa was adopted.

It was observed from the experiments that portions of the reinforcing bars where strain gage were

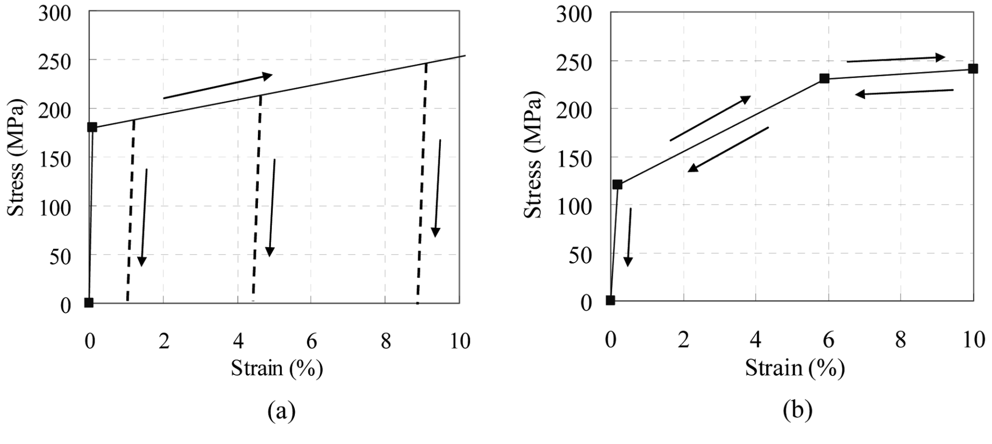

(a) (b)

Fig. 13 Constitutive models for the reinforcing bars: (a) steel bar and (b) SMA bar attached did not necessarily yield. It was inferred from this result that the behavior of the reinforced specimens was controlled by yielding concentrated at the threaded portions of the reinforcing bars. To simulate this behavior, reduced section truss elements of 3 mm diameter were used at the bottom and top portion of the reinforced specimens. Also in case of the SMA-RM model, reduced section truss element was used at the 3rd mortar level from the bottom where a couple, or a long nut, was attached. The length of the reduced section reinforcing bar was kept at 10 mm for the bottom threaded portion, and 5 mm for the threaded portion where the coupler was attached. These values were determined to make the mesh as simple as possible. The threaded portions for the SMA-RM model are shown in Fig. 11. One threaded portion was located at the bottom where the nut was connected. And the other portion was located at the 3rd mortar level from the bottom at the coupler's location. Note that, in case of the ST-RM model, no coupler was used and that threaded portions were located only at the bottom and top of the brick wall specimen.

3.2 Results

3.2.1 URM Specimen

Fig. 14 shows the horizontal resisting force-rotation angle plot for the experimental as well as numerical observations. The plots show good comparable response. The FE response simulated well the two distinct phases; the pre- and post-peak stages. Simulating the decrement in the resisting force in the post-peak stage was possible by including geometric nonlinearity. The numerical results also agreed well with the theoretical rigid body assumption as shown in Fig. 14 (b).

3.2.2 ST-RM Specimen

Fig. 15 shows the comparison of the responses of the ST-RM specimen. In Figs. 15(a) and 15(b), the pre- and post-peak behavior of the FE model matched the experimental results and the theoretical predictions reasonably well. The initial peak strength, attributed to tensile cracking of mortar bed joint, for the FE model was in the lower side. Large variability in the tensile strength

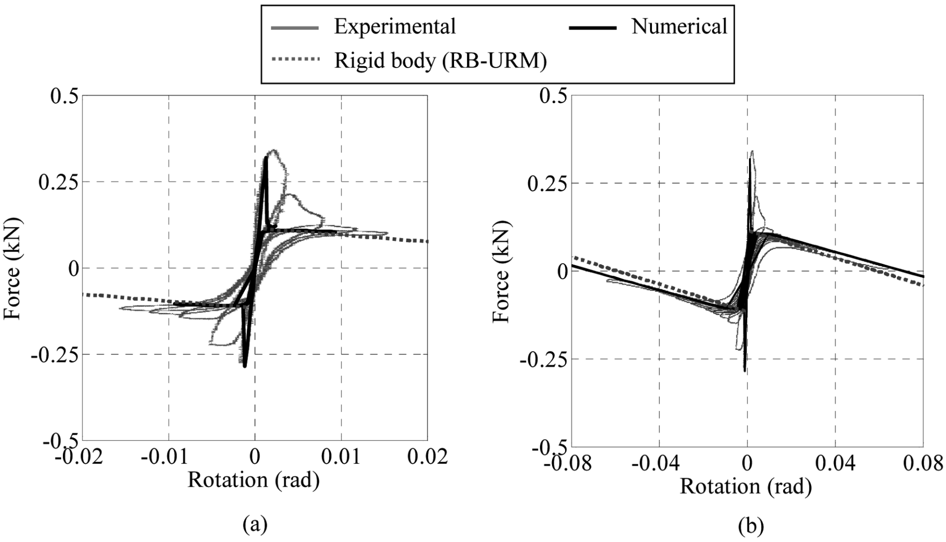

(a) (b)

Fig. 14 Comparison for the URM specimen: (a) $\theta_a < 1/70$ radian and (b) $\theta_a > 1/70$ radian

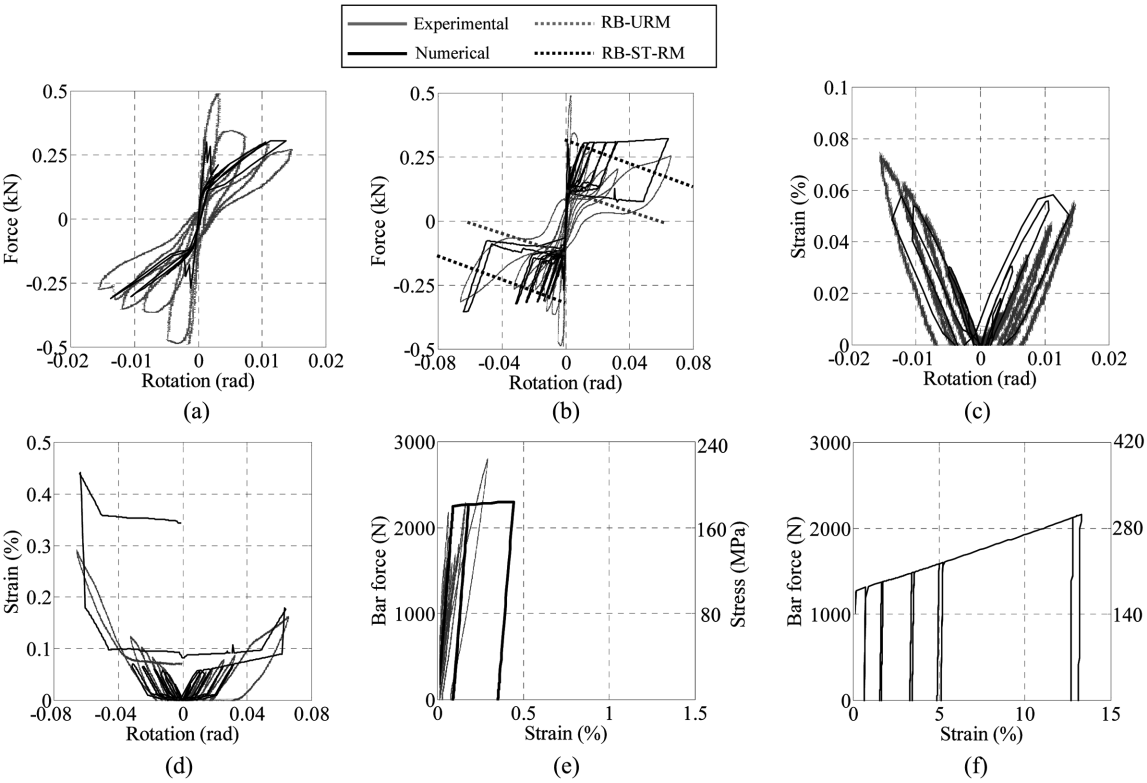

(a) (b) (c)

(d) (e) (f)

Fig. 15 Comparison for the ST-RM specimen: (a) force-rotation relation for $\theta_a < 1/70$ radian, (b) force-rotation relation for $\theta_a > 1/70$ radian, (c) strain-rotation relation for $\theta_a < 1/70$ radian, (d) strain-rotation relation for $\theta_a > 1/70$ radian, (e) bar force-strain relation at strain measured portion and (f) bar force-strain relation at threaded portion

seems to be the reason of the lower prediction. The FE results predicted reasonably well the more important post-cracking phase as seen in Figs. 15(a) and 15(b). In Fig. 15(b), pinching phenomenon was clearly observed for the FE results during unloading phase as well. Figs. 15(c) and 15(d) show the comparison of the strain history prediction with the strain gage data for $\theta_a < 1/70$ radian and $\theta_a > 1/70$ radian respectively. No significant residual deformation was observed from the experiment with the exception of the last cycle, where residual strain of 0.06% was recorded. Numerical results in Figs. 15(c) and 15(d) agreed well with the experimental observations with the exception of the last 2 cycles. As shown in shown in Fig. 15(e), the portion of reinforcing bar where the strain gage measurement was made primarily worked in its elastic range while yielding concentrated at the threaded portion of the reinforcing bars as shown in Fig. 15(f). Note that, in Fig. 15(e), the experimentally observed bar force F_p^{RM} was obtained inversely by Eq. (5) making the rigid body assumption and using the horizontal restoring force F_R measured.

$$F_p^{RM} = \frac{2}{t}F_R(h+t\theta) - \left(1-\frac{2h}{t}\theta\right)mg \qquad (5)$$

Fig. 16 illustrates the mechanism of the pinching phenomenon. Three different loading instants are shown in Fig. 16(a) represented by Point B at $\theta = 1/18$ radian, Region A, and Point C at $\theta = -1/18$ radian. Up to Point B, with increasing the rotation angle, the horizontal resisting force also

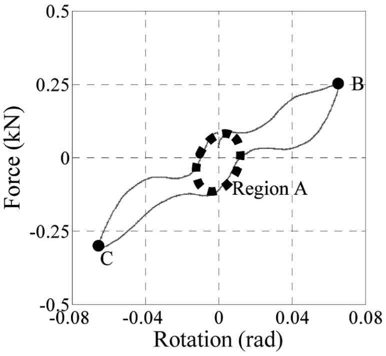

(a)

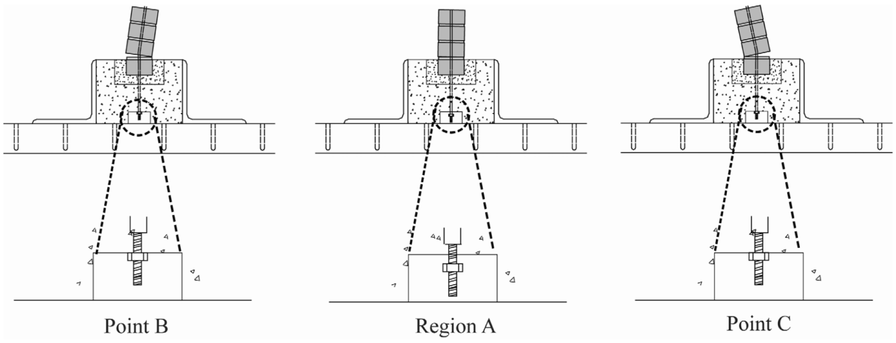

Deformed shapes at the bottom of specimen

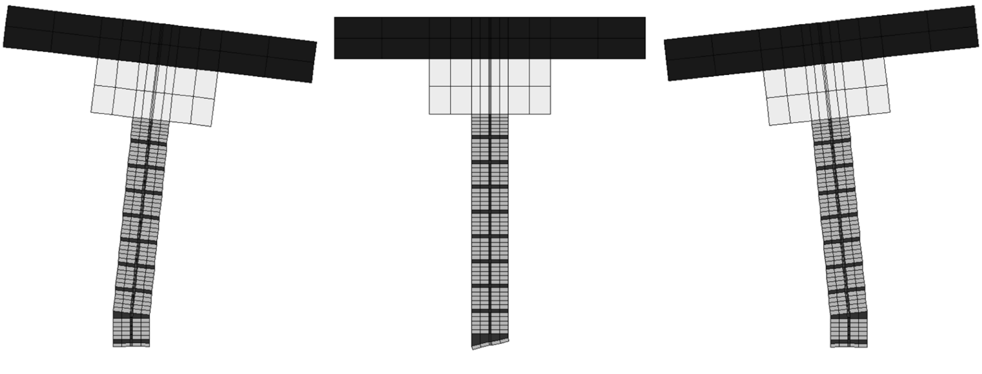

(b) θ = +1/18 rad (c) θ = 0 rad (d) θ = -1/18 rad

Deformation scale = 1.5 Deformation scale = 5 Deformation scale = 1.5

Fig. 16 Mechanism observed for the ST-RM specimen: (a) typical distinct phases in the force rotation angle history (10th cycle), (b) deformed shape at θ_a = +1/18 radian, (c) deformed shape at θ_a = 0 radian and (d) deformed shape at θ_a = -1/18 radian

increased as shown in Fig. 16(a). With the release of the load from Point B, unloading took place almost linearly up to the rotation angle of 0.04 radian. From this point on, pinching phenomenon in the wall was observed. In Region A, rocking resistance due to gravity was observed, which can be represented by the rigid body assumption for the URM model. The reinforcing bars were allowed to deform almost freely at the bottom of the wall specimen which resulted in the rocking response observed. The deformed shape of the numerical model, as shown in Fig. 16(c), shows the crack occurring at the nut interface. In the negative loading towards Point C, the gap between the nut and the concrete block closed, and the crack was initiated at the 1st mortar joint level as shown in Fig. 16(d). Afterwards, the horizontal resisting force increased with increasing the rotation angle up to Point C. To summarize, it can be seen from the numerical results that the whole mechanism during the loading history was primarily governed by the plastic residual deformation concentrated in the threaded region of the steel reinforcing bar.

3.2.3 SMA-RM specimen

The horizontal resisting force-rotation relations obtained from the FE model are compared with the experimental results and the theoretical predictions as shown in Figs. 17(a) and 17(b). Both plots show comparable pre- and post-peak responses. Fig. 17(b) shows constant horizontal resisting force for $\theta > 0.04$ radian representing yielding of the SMA bars. During the subsequent unloading, due to superelastic property of SMA bars, comparatively stable response was observed with no pinching phenomenon. Figs. 17(c) and 17(d) show the comparisons of the strain-rotation angle relationship. The tri-linear elastic model adopted for the SMA bar represented the experimentally observed strain history reasonably well. The strain gage data observed experimentally and computed numerically both exhibited no residual strain in any of the loading cycles. In Fig. 17(e), the experimentally

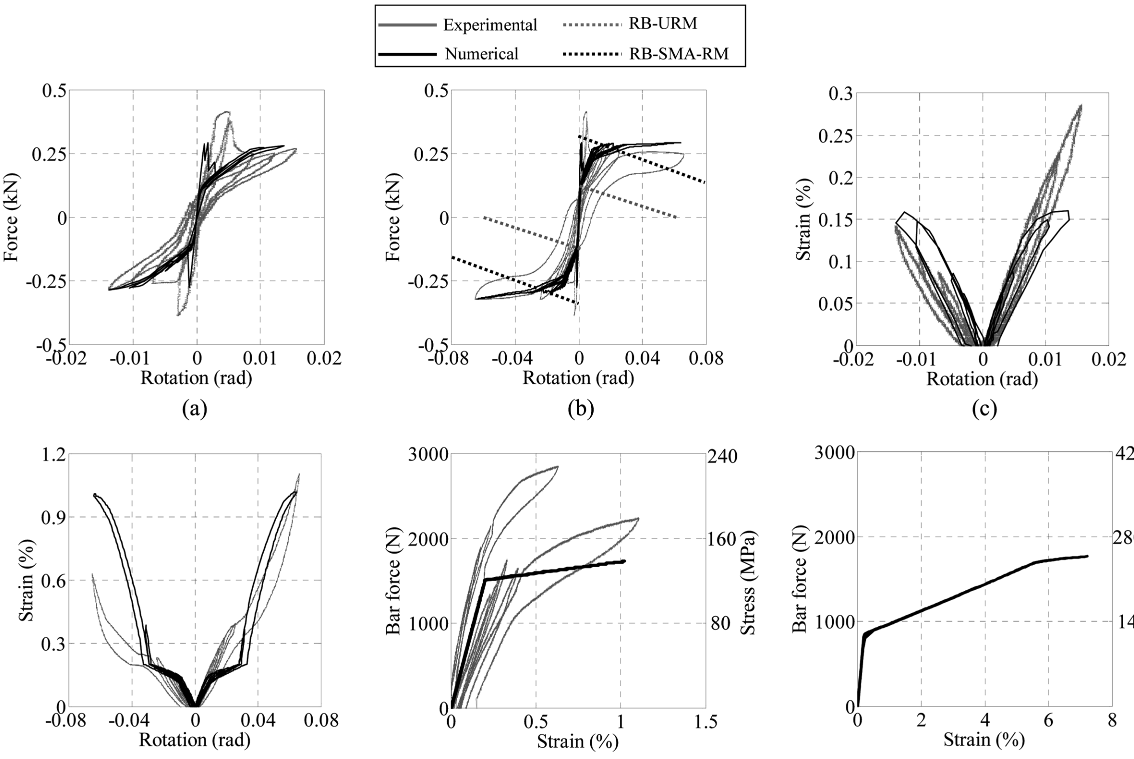

Fig. 17 Comparison for the SMA-RM specimen: (a) force-rotation relation for $\theta_a < 1/70$ radian, (b) force-rotation relation for $\theta_a > 1/70$ radian, (c) strain-rotation relation for $\theta_a < 1/70$ radian, (d) strain-rotation relation for $\theta_a > 1/70$ radian, (e) bar force-strain relation at strain measured portion and (f) bar force-strain relation for threaded portion

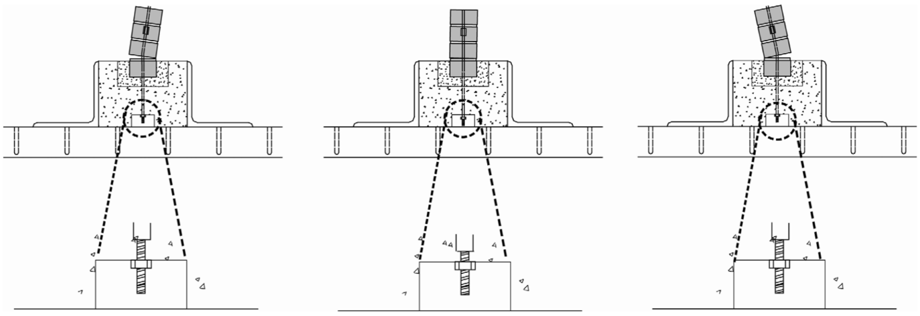

Deformed shapes at the bottom of specimen

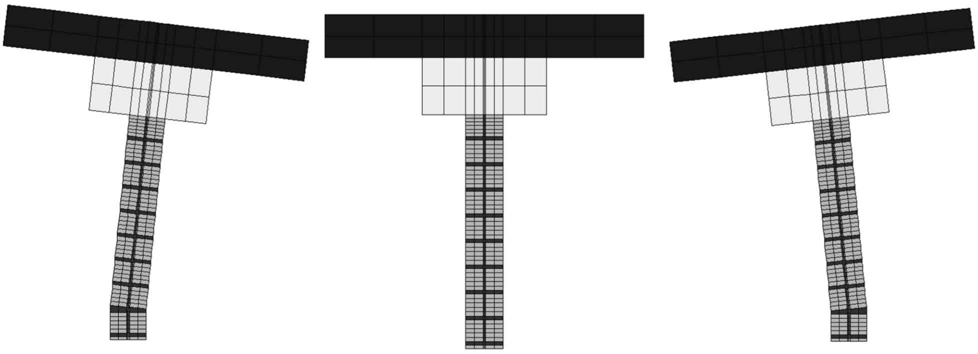

(a) $\theta = +1/18$ rad
Deformation scale = 1.5

(b) $\theta = 0$ rad
Deformation scale = 5

(c) $\theta = -1/18$ rad
Deformation scale = 1.5

Fig. 18 Deformed shapes for the SMA-RM specimen: (a) $\theta_a = +1/18$ radian (b) $\theta_a = 0$ radian and (c) $\theta = -1/18$ radian

observed force in the SMA bar was obtained by Eq. (5). From the FE computation, the strain observed at the threaded portion of the SMA bar showed clear sign of yielding beyond 0.2% strain as shown in Fig. 17(f).

Fig. 18 shows the response observed at the bottom of the SMA-RM model obtained through the numerical simulation. Here, the results are shown for three different instants of loading, $\theta = 1/18$ radian, $\theta = 0$ radian and $\theta = -1/18$ radian. For $\theta = 1/18$ radian, the out-of-plane loading caused cracking at the 1st mortar joint level from the bottom as shown in Fig. 18(a). With the initiation of unloading phase, the resisting force decreased gradually with the decrement in rotation angle with no sign of pinching due to absence of residual deformation of the SMA reinforcing bar. The crack at the nut interface was not seen at the instant of $\theta = 0$ radian as shown in Fig. 18(b). In the negative loading, for $\theta = -1/18$ radian, again the crack at the 1st mortar joint level from the bottom was observed as shown in Fig. 18(c).

3.3 Discussions

As shown in the previous sections, the behavior of the ST-RM and SMA-RM specimens are considerably different. Nevertheless, the increments in strength and ductility are almost similar in both specimens. And the differences in the response of the specimens are not very large especially in the small deformation range. As a result, the strengths of the use of SMA reinforcing bars over steel bars may be argued. This section discusses this issue in detail, and also discusses some other issues concisely.

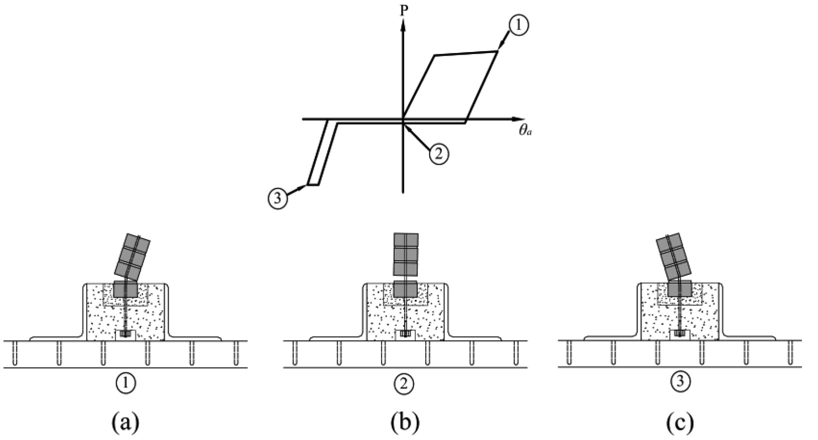

Fig. 19 Schematic representations for mechanisms of steel reinforced specimens with reinforcing bars fixed at the bottom at: (a) maximum positive loading post yield of reinforcing bar, (b) initial straight position and (c) maximum negative loading

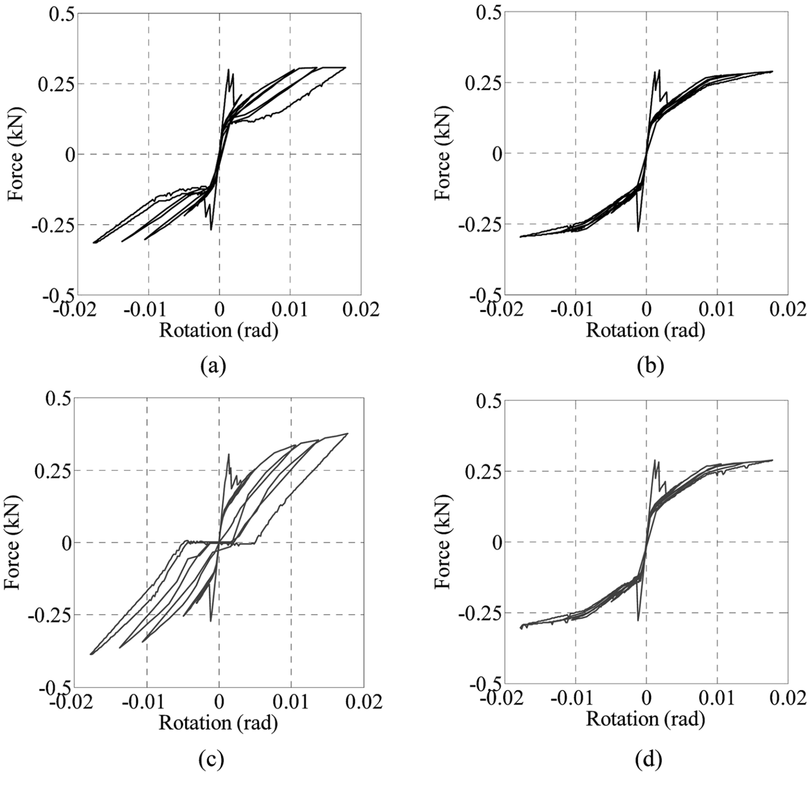

(a)

(b)

(c)

(d)

Fig. 20 Force rotation relation for the non-fixed and fixed base models: (a) ST-RM, (b) SMA-RM, (c) ST-RM^{FB} and (d) SMA-RM^{FB}

As described in the preceding sections, reinforcing bars were not fixed and allowed to deform almost freely at the bottom of the wall specimen in the present experiment, while in actual practice reinforcing bars are usually fixed at the bottom. As a result, the experimental observations in the present study are different in some points from those in more practical settings (Button and Mayes 1992, Tomazevic 1995). When reinforcing bars are fixed at the bottom of the wall as shown in Fig. 19, pinching is caused by inelastic elongation of reinforcing bars around the crack at the 1st bed joint. In this case, the crack at the bed joint does not close and the reinforcing bar works as a pin support when the wall returns to initial straight position as shown in Fig. 19(b). The stiffness around the initial position becomes nearly zero after yielding of reinforcing bars. On the other hand, when reinforcing bars are not fixed as in the present experiment, the crack at the 1st bed joint closes when the rotation angle returns to zero as shown in Fig. 16(c). This leads to rocking resistance due to gravity as depicted in Fig. 16(a).

In order to examine the response of reinforced walls to show the above behavior in a more practical setting, FE models were developed wherein reinforcing bars are fixed at the bottom of the wall specimen. SMA-RM^{FB} and ST-RM^{FB} represent the corresponding SMA reinforced and steel reinforced FE models where reinforcing bars are fixed at the bottom of the wall specimen. Comparisons between the non-fixed and fixed models in Fig. 20 show contrasting characteristics. As shown in Figs. 20(a) and 20(c), the tangent stiffness around the initial position becomes nearly zero in case of ST-RM^{FB} model, while it does not in case of ST-RM model. The difference can be clearly seen even in the small deformation range. On the other hand, as shown in Figs. 20(b) and 20(d), the stiffness around the initial position for SMA-RM and SMA-RM^{FB} is always high and similar regardless of the condition of fixing the reinforcement at the bottom. Fig. 21 shows comparisons of typical post yield cyclic responses, and Fig. 22 illustrates the FE deformed shapes for all the models at the initial straight position at the end of corresponding post yield cycles of Fig. 21. In Fig. 21(a), the difference between responses of ST-RM and ST-RM^{FB} models in their post yield behavior can be clearly seen with ST-RM model showing rocking response around the initial position with crack at the nut interface as shown in Fig. 22(a). ST-RM^{FB} model in Fig. 22(c) shows crack at the mortar bed joint as depicted schematically in Fig. 19. On the other hand SMA-RM and

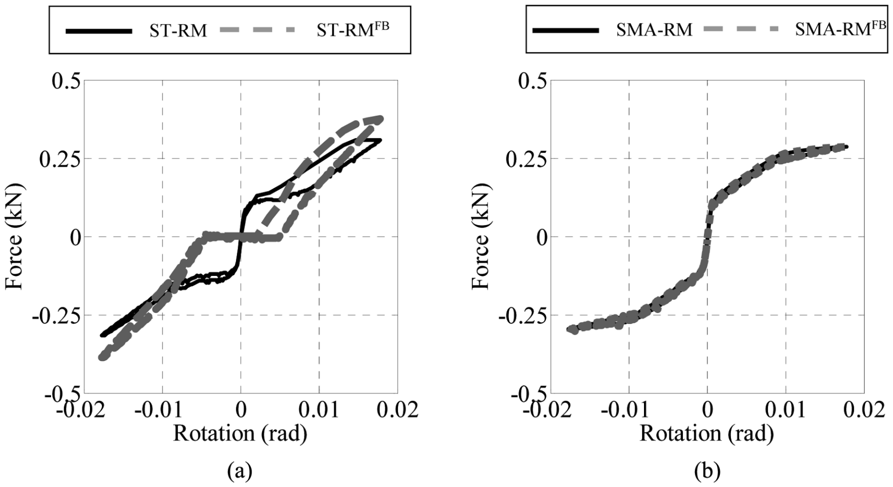

(a) (b)

Fig. 21 Comparison between typical post yield cycle for the non-fixed and fixed base models: (a) ST-RM and ST-RM^{FB} and (b) SMA-RM and SMA-RM^{FB}

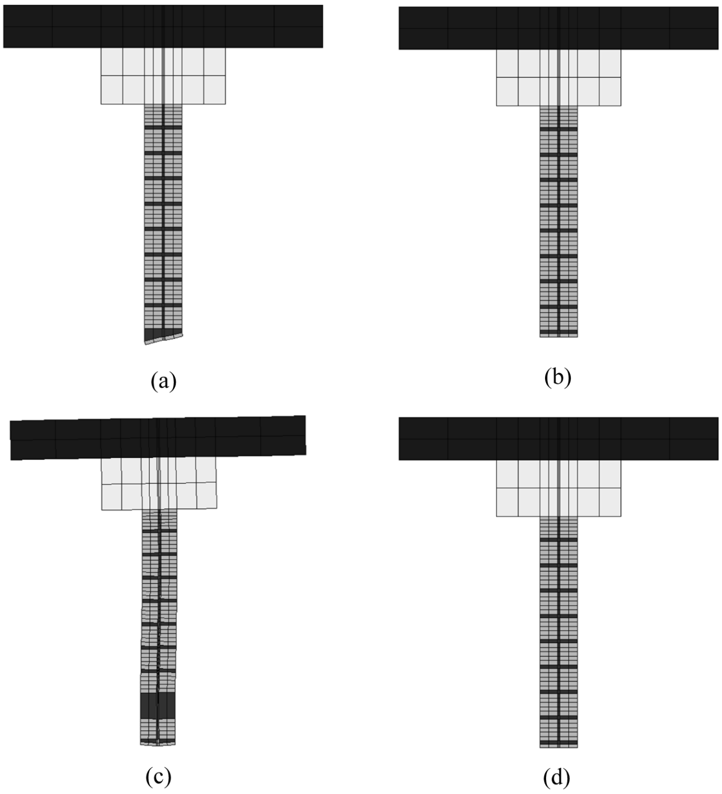

Fig. 22 FE deformed shapes around initial equilibrium position of $\theta_a = 0$ radian for the non-fixed and fixed base models: (a) ST-RM, (b) SMA-RM, (c) ST-RM^{FB} and (d) SMA-RM^{FB}

SMA-RM^{FB} models show no significant difference in their force-rotation relation as shown in Fig. 21(b) and both show no cracks with the release of loads at the initial straight position as illustrated in Figs. 22(b) and 22(d) respectively. These figures clearly demonstrate the effectiveness of SMA bars over steel bars as reinforcing elements in a more practical setting.

Other than the issue of fixing reinforcing bars at the bottom, the following discussions can be made on the issues that arose in the experiments and FE modeling:

1. Dowel action: Dowel action of reinforcing bars was neglected in FE modeling by modeling reinforcing bars using truss elements. The reasonably good agreements between the results of the experiments and numerical simulations validate this assumption.
2. Bond slip: Slip between the steel reinforcing element and masonry element was controlled mainly by whether the bottom of the reinforcing bar was fixed or non-fixed as discussed previously. A pronounced amount of slip with subsequent crack at the nut interface for non-fixed base ST-RM model can be seen in Fig. 22(a) caused by inelastic elongation of reinforcing bars. The superelastic property of SMA bars used prevented any slip to occur in case of SMA-RM models shown in Figs. 22(b) and 22(d). Additionally in a more practical setting with fixed base ST-RM^{FB} models, slip between reinforcing elements and masonry elements was dominated by mortar bed joint crack as shown in Fig. 22(c).
3. Size effect: In this study, reduced scale specimens were used in the experiments. Although real-scale models can be easily made using FE models developed in this study, further study is still

necessary on the size dependence of constitutive relations in Cu-Al-Mn SMA bars and in mortar joints to reliably predict the response of actual retrofitted masonry structures.

4. Repetition of loading cycle: In both the experiments and FE modeling, loading was applied only once at each amplitude of rotation angle. It may be argued how repetition of loading at the same amplitude affects the response. Although further study is necessary to answer this question clearly, it is expected that the effect is negligible in the URM and SMA-RM specimens because the effect of repetition of loading cycle becomes significant only when inelastic deformation occurs in reinforcing bars. On the other hand, the difference of response between the 1st and 2nd cycles would be significant in the ST-RM specimen while the differences after the 2nd cycle would be negligible.

4. Conclusions

An experimental study has been conducted to investigate the applicability of newly developed Cu-Al-Mn SMA bars to seismic retrofitting of historical URM constructions. Displacement controlled quasi-static tests were done on the URM, ST-RM, and SMA-RM wall specimens under cyclic out-of-plane loading. FE models were generated with simplified micro modeling strategy, where bricks, mortar joints, and reinforcing bars were represented by continuum elements, interface elements, and truss elements, respectively. Within the scope of the study, the following conclusion can be drawn:

(1) Both the ST-RM and SMA-RM specimens showed significant increment both in strength and ductility as compared to the URM specimen. The ST-RM specimen showed pinching phenomenon in the large deformation range while the SMA-RM specimen did not. These results demonstrate the applicability and superiority of the present Cu-Al-Mn SMA bars to retrofitting URM walls as a partial replacement of steel bars.

(2) FE models were developed and calibrated to simulate the experimental results. The developed FE models predicted reasonably well the complete history of all the specimens. Through the FE analysis of the ST-RM specimen, it was shown that the inelastic elongation of the steel bars was the main source of pinching. It was also shown that the superelastic property of the SMA bars was effective to avoid pinching.

(3) It was demonstrated that, if reinforcing bars are fixed at the bottom of the wall specimen, the ST-RM model showed pinching phenomenon even in the small deformation range while the SMA-RM model did not. This result highlights the superiority of the retrofitting of URM walls by SMA bars in a more practical setting.

Acknowledgements

This research was supported by Grant-in-Aid for Scientific Research (B) No. 20360253 and by the Global COE Program, provided by the Japan Society for the Promotion of Science (JSPS). Part of this research was also supported by International Copper Association (ICA). The financial assistance is gratefully acknowledged. The half-scale bricks used in this study were originally produced in the early 1980s by Prof. em. Minoru Wakabayashi of Kyoto University and Prof. em. Takeshi Nakamura of Kyoto Institute of Technology. Prof. Kiyotaka Morisako and Prof. Satoko Kitao of Kyoto Institute of Technology kindly provided the bricks for the experiment. Mr.

Nobutoshi Yoshida and Mr. Ippei Ibarada undertook the experimental works. The comments and questions from the reviewers led to significant improvement of the draft of this paper. All the supports mentioned above are highly acknowledged.

References

Abrams, D., Smith, T., Lynch, J. and Franklin, S. (2007), "Effectiveness of rehabilitation on seismic behavior of masonry piers", *J. Struct. Eng. - ASCE*, **133**(1), 32-43.

Araki, Y., Endo, T., Omori, T., Sutou, Y., Koetaka, Y., Kainuma, R. and Ishida, K. (2010), "Potential of superelastic Cu-Al-Mn alloy bars for seismic applications", *Earthq. Eng. Struct. Dyn.*, **40**(1), 107-115.

ASTM (2007), *Annual book of ASTM standards. Section four, construction, volume 04.05, chemical-resistant nonmetallic materials; vitrified clay pipe; concrete pipe; fiber-reinforced cement products; mortars and grouts; masonry; precast concrete*, ASTM International, West Conshohocken, PA.

Button, M.R. and Mayes, R.L. (1992), "Out-of-plane seismic response of reinforced masonry walls", *J. Struct. Eng. - ASCE*, **118**(9), 2495-2513.

Christis, Z.C., Andreas, S., Themos, D. and Karim, H. (2008), "Application of shape memory alloy prestressing devices on an ancient aqueduct", *Smart Struct. Syst.*, **4**(2), 261-278.

DesRoches, R. and Smith, B. (2004), "Shape memory alloys in seismic resistant design and retrofit: a critical review of their potential and limitations", *J. Earthq. Eng.*, **8**(3), 415-429.

DIANA (2008), *DIANA user's manual release 9.3*, TNO DIANA BV, Delft, The Netherlands.

Ehsani, M.R., Saadatmanesh, H. and Velazquez-Dimas, J.I. (1999), "Behavior of retrofitted URM walls under simulated earthquake loading", *J. Compos. Constr.*, **3**(3), 134-142.

El-Borgi, S., Neifar, M., Ben, J. M., Cherif, D. and Smaoui, H. (2008), "Use of copper shape memory alloys in retrofitting historical monuments", *Smart Struct. Syst.*, **4**(2), 247-260.

ElGawady, M.A., Lestuzzi, P. and Badoux, M. (2004), "A review of conventional seismic retrofitting techniques for URM", *Proceedings of 13th International Brick and Block Masonry conference*, Amsterdam, Netherland, July.

Eurocode 8 (2004), *Eurocode 8: Design of structures for earthquake resistance - Part 1: General rules, seismic actions and rules for buildings*, EN 1998-1:2004, European Committee for Standardization, Brussels.

Griffith, M.C., Lam, N.T.K., Wilson, J.L. and Doherty, K. (2004), "Experimental investigation of unreinforced brick masonry walls in flexure", *J. Struct. Eng. - ASCE*, **130**(3), 423-432.

Indirli, M., Castellano, M., Clemente, P. and Martelli, A. (2001), "Demo-application of shape memory alloy devices: the rehabilitation of the S. Giorgio Church Bell-Tower", *Proceedings of SPIE*, California, March.

Karantoni, F.V. and Fardis, M.N. (1992), "Effectiveness of seismic strengthening techniques for masonry buildings", *J. Struct. Eng. - ASCE*, **118**(4), 1884-1902.

Lourenco, P.B. and Rots, J.G. (1997), "Multisurface interface model for analysis of masonry structures", *J. Struct. Eng. - ASCE*, **123**(7), 660-668.

Mazzolani, F.M. and Mandara, A. (2002), "Modern trends in the use of special metals for the improvement of historical and monumental structures", *Eng. Struct.*, **24**(7), 843-856.

Martelli, A. (2008), "Recent progress of application of modern anti-seismic systems in Europe – Part 2: energy dissipation systems, shape memory alloy devices and shock transmitters", *Proceedings of the 14th World Conference on Earthquake Engineering*, Beijing, China, October.

Oliveira, D.V., Lourenco, P.B. and Roca, P. (2006), "Cyclic behaviour of stone and brick masonry under uniaxial compressive loading", *Mater. Struct.*, **39**(2), 247-257.

Paret, T.F., Freeman, S.A., Searer, G.R., Hachem, M. and Gilmartin, U.M. (2008), "Using traditional and innovative approaches in the seismic evaluation and strengthening of a historic unreinforced masonry synagogue", *Eng. Struct.*, **30**, 2214-2126.

Plecnik, J., Cousins, T. and O'conner, E. (1986), "Strengthening of unreinforced masonry buildings", *J. Struct. Eng. - ASCE*, **112**(5), 1070-1087.

RILEM (1994), *RILEM Technical recommendations for the testing and use of construction materials*, Taylor & Francis, New York.

Song, G., Ma, N. and Li, H.N. (2006), "Applications of shape memory alloys in civil structures", *Eng. Struct.*, **28**, 1266-1274.

Sutou, Y., Omori, T., Wang, J.J., Kainuma, R. and Ishida, K. (2003), "Effect of grain size and texture on superelasticity of Cu-Al-Mn-based shape memory alloys", *J. Phys. IV*, **112**, 511-514.

Sutou, Y., Omori, T., Yamauchi, K., Ono, N., Kainuma, R. and Ishida, K. (2005), "Effect of grain size and texture on pseudoelasticity in Cu-Al-Mn-based shape memory wire", *ACTA Mater.*, **53**(15), 4121-4133.

Tomazevic, M. (1995), *Earthquake-resistant design of masonry buildings*, Imperial College Press, London.

Willis, C.R., Seracino, R. and Griffith, M.C. (2010), "Out-of-plane strength of brick masonry retrofitted with horizontal NSM CFRP strips", *Eng. Struct.*, **32**(2), 547-555.

IT